Ru-Doping of P2-NaxMn0.75Ni0.25O2-Layered Oxides for High-Energy Na-Ion Battery Cathodes: First-Principles Insights on Activation and Control of Reversible Oxide Redox

ACS APPLIED ENERGY MATERIALS

www.acsaem.org Article

Ru-Doping of P2-$Na_xMn_{0.75}Ni_{0.25}O_2$-Layered Oxides for High-Energy Na-Ion Battery Cathodes: First-Principles Insights on Activation and Control of Reversible Oxide Redox Chemistry

Arianna Massaro, Aniello Langella, Claudio Gerbaldi, Giuseppe Antonio Elia, Ana B. Muñoz-García,* and Michele Pavone*

Cite This: *ACS Appl. Energy Mater.* 2022, 5, 10721−10730 Read Online

ACCESS | Metrics & More | Article Recommendations | Supporting Information

ABSTRACT: Design and development of high-energy, efficient, and structurally stable positive electrodes for Na-ion batteries (NIBs) have recently been focusing on layered transition metal oxides (Na_xTMO_2, $0 < x < 1$). When doped with late transition metals, the redox reactions ensuring the charge compensation upon Na^+ removal can rely on the direct participation of anionic chemistry, with encouraging outcomes in terms of both energy density and power. However, the control of reversible O^{2-}/O^- reactions is still a major issue, as the undesired release of O_2 can lead to detrimental effects on cathode capacity and overall cell stability. The fine-tuning of metal−oxygen bond covalency has recently emerged as a promising strategy toward the reversible access of oxygen redox. Following the route paved by Ru-based Li-rich cathode materials, we hereby present a first-principles investigation of a Ru-doped Na_xTMO_2 (TM = Ru, Ni, and Mn) system and the related structural and electronic properties of interest for NIB applications. We aim to dissect the specific role of each element sublattice in compensating the electronic charge along desodiation, with a major focus on the anionic contribution. The oxygen activity is addressed in the high-voltage range (i.e., $x_{Na} = 0.25$), and the underlying mechanism is derived from PBE + U(-D3BJ) calculations. We also discuss the effects of Mn deficiency as a suitable site for the formation of low-energy superoxide species via preferential breaking of the Ni−O bond. Conversely, breaking a Ru−O bond is unlikely to occur, which assesses the key role of the Ru dopant in stabilizing the oxide lattice and enabling the desired reversible conditions. Our results also highlight the oxygen vacancy formation energy as an effective descriptor for different activities toward the $O^{2-}/O^-/O_2$ evolution. All these theoretical insights can be useful to drive further experimental efforts toward the optimal design of efficient and high-energy NIB cathodes with enhanced practical reversible capacity.

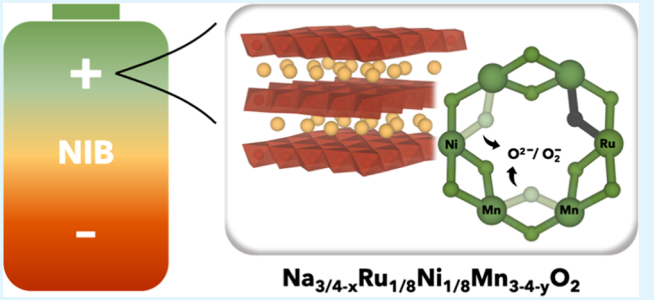

KEYWORDS: *sodium-ion battery, high-energy cathode, anionic redox activity, Ru doping, DFT calculation*

INTRODUCTION

The perspective of a sustainable society based on a green economy strictly relies on the development and exploitation of energy storage technologies.[1] By capturing and delivering clean energy from renewables, large-scale units integrated to smart electrical grids can reduce imbalances between the demand and the production of energy for both domestic and industrial purposes.[2] Several aspects are key for the rapid entry in the market, such as cost, safety, and recyclability. Post-lithium batteries based on cheap and widespread raw materials and fabricated in all-solid-state configurations would meet the market requirements and thus have been quickly emerging as a promising solution toward the green energy transition.[3,4] However, addressing the device performance parameters, such as energy density, cycle life, and long-term stability, still represents a great challenge from the scientific point of view.[5] Great efforts from the worldwide research community are being dedicated to the rational design of efficient component materials and the assessment of main working processes.[6−8]

Among many other technologies, Na-ion batteries (NIBs) would represent a viable and convenient alternative to their Li-ion counterparts for large-scale applications, and their development could benefit from similar operating principles.[4] However, novel electrode materials need to be designed with a similar or even superior performance toward ion intercalation/deintercalation reactions compared to state-of-the-art Li-ion batteries (LIBs).[6−8] At the cathode side, structurally stable

Received: May 12, 2022
Accepted: August 10, 2022
Published: September 1, 2022

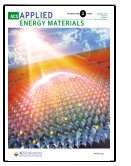

compounds, able to operate at high voltage, thus allowing for high-energy density devices, are at the forefront of this research field.[9−11] Layered transition metal oxides (Na_xTMO_2, $0 < x < 1$) have been attracting great attention due to enhanced electrochemical properties.[11−14] The crystalline structure features TMO_2-based layers alternated with Na ones that act as open diffusion pathways for efficient Na^+ uptake and storage.[14] Within Na channels, the crystalline site can feature either an octahedral or trigonal prismatic coordination, which are usually defined as O or P, respectively.[13] The oxygen stacking also gives rise to different lattice symmetries, labeled as 2 or 3, according to the number of TMO_2 layers contained in the unit cell.[13] In the energy material community, the major interest in the P2 polymorphs arises from their higher capacity and better cycle life due to larger trigonal prismatic sites facilitating Na^+ transport.[14] The Na^+ removal during cathode charge usually hinges on the reversible TM redox couples. In the case of early-TM-based oxides, O 2p states lie well below the TM d states, leading to a predominantly metallic character at the Fermi level, and the transition metals mainly undertake the burden of the redox reaction, that is, the cationic redox chemistry.[15] As going from early to late transition metals or to higher valence metal states, the electronegativity is increased, which enables larger overlapping between TM d and O p states and allows more covalent interactions.[16] In this scenario, the oxygen electron density can directly participate in charge compensation, giving rise to the so-called anionic redox chemistry.[17,18] Enabling reduction/oxidation of the oxide sublattice pushes the cathode capacity beyond the limit of TM redox potentials and leads to further improvements in both the amount of energy stored and the power delivered.[19−25] Unfortunately, an uncontrolled oxidation process can lead to the formation of unbound molecular oxygen, with detrimental effects on the overall capacity and long-term stability during cycling.[21−24] Several strategies are being pursued to prevent such undesired reactions, and theoretical studies can reinforce the experimental efforts to this end by enlightening the origin of anionic redox at the atomistic scale.[25−29] From a general perspective, the fine-tuning of TM doping is required for the activation and control of reversible O^{2-}/O^- reactions. Playing with atom substitution at the TM site can be a tricky task, as the electrochemical properties are very sensitive to the cation chemical nature.[30] Substituting TM for d^0 or alkali metals, introducing TM deficiency using cation-disordered structures as well as increasing the TM−O bond covalency are among the most investigated strategies to suppress irreversible O_2 loss.[26,31−33] In particular, the employment of TM-defective oxides has attracted consideration as a viable strategy to enable anionic redox and thus enhance the specific capacity of layered oxides due to the emergence of nonbonding O 2p states.[32] However, the presence of a TM vacancy in the bulk lattice can represent a suitable site to accommodate the reactive oxygen species resulting from the uncontrolled anionic redox.[21,28] In general, the development of efficient NIB cathodes could benefit from advances and knowledge already attained for LIB analogues. The relationship between TM composition and reversible anionic redox in Li-rich layered oxides (Li_2TMO_3) has been extensively reported and elucidated.[34−38] By correlating the oxygen frequency shifts observed in the phonon density of states along $Li_{2-x}TMO_3$ delithiation (TM = Ru, Ni, and Mn) to the nature of the TM−O chemical bond, Shao-Horn and co-workers have unveiled that lattice dynamics can affect both ion mobility and structural stability; they clarified that these effects can be successfully restrained in highly covalent TM oxides.[35,37] The presence of Ru in such Li-rich materials seems to be a key enabler to accomplish a reversible access of oxygen redox.[39] Not only do the electronic signatures of reversible O−O coupling in $Li_{2-x}RuO_3$ at ∼4.2 V versus Li^+/Li represent direct evidence of lattice oxygen redox activated at high voltage,[36] but also the oxygen dimerization mechanism in Ru-doped Li_2TMO_3 is shown to be hampered compared to other TM doping.[37,38] Despite being few, the scientific reports on the use of Ru-doped NIB cathodes have shown promising results.[40] Of course, from the perspective of sustainability and low-cost, it is crucial to find an optimal balance between the Ru amount employed and the possible benefits on the overall cell performances. From the above-mentioned considerations, we think that further investigation based on first-principles methods can shed light on the oxygen redox in Ru-doped Na_xTMO_2 and drive the experimental efforts toward the fine-tuning of high-energy cathodes working in reversible conditions. In our previous work, we have addressed the charge compensation exerted by the oxide sublattice at a high voltage (i.e., low Na content) in Na_xTMO_2 systems (TM = Ni, Mn, and Fe):[28,29] while molecular oxygen can be released via preferential breaking of labile Ni−O bonds, Fe doping is shown to effectively suppress the O_2 loss, which still enables the activation of anionic redox (e.g., the formation of low-energy superoxide species) due to introduction of mild TM−O bond strength. In this way, experimental evidence of a high-voltage plateau (∼4.5 V vs Na^+/Na) recorded during the first charge cycle of $Na_{0.78}Ni_{0.23}Mn_{0.69}O_2$ or the reversible behavior observed at ∼4.3 V versus Na^+/Na for $Na_{2/3}Fe_{2/9}Ni_{2/9}Mn_{5/9}O_2$ could have been clarified from first principles.[22,23] We have also highlighted that oxygen vacancy formation energies can be used to quantify the tendency of a given TM composition to stabilize/destabilize the oxide sublattice.

Following this path, we hereby report a thorough investigation of $Na_xRu_{1/8}Ni_{1/8}Mn_{3/4}O_2$ (NRNMO) at different sodiation stages. This stoichiometry complies with the doping ratio from former case-studies from our research group[28,29] and is still comparable to the one reported in the literature, for example, $Na_{0.75}Ni_{1/3}Ru_{1/6}Mn_{1/2}O_2$.[40] It is worth mentioning that the Ru doping amount proposed herein is rather small, and it is shown to be beneficial for controlling the oxygen redox reactions in such high-energy cathodes. Our computational-assisted analysis dissects the contribution of each element sublattice along desodiation so as to assess the role of Ru doping in preventing the O_2 release and, thus, improving the reversible capacity. We also investigate the role that Mn deficiency plays on both structural and electronic features of NRNMO material in order to discuss the effects on the electrochemical properties and to suggest possible design strategies for high-energy Ru-based cathodes. It is worth recalling that, on the one hand, TM-deficient phases in layered oxides are foreseen to enable the desired anionic chemistry and thus enhance the cathode specific capacity, and on the other hand, the TM-vacant site can host unwanted oxygen reactive species. The effective design of a high-energy NIB cathode able to work in reversible conditions should not neglect the in-depth investigation of the structure−property relationship in bulk TM-deficient phases as well as the mechanism underlying the oxygen redox activity. Structural evolution and redox properties of stoichiometric and Mn-deficient NRNMO are described within the PBE + U(-D3BJ) approach as a function

https://doi.org/10.1021/acsaem.2c01455
ACS Appl. Energy Mater. 2022, 5, 10721−10730

of the sodiation degree. The oxygen activity is addressed as the oxide-to-dioxygen transition near the Mn deficiency. By comparing oxygen vacancy formation energies in various chemical environments featured in NRNMO, we could unveil the role of TM−O bond strength in determining the superoxide formation mechanisms. Our results point out that Ru doping is crucial to stabilize the oxide lattice and prevent the loss of molecular oxygen. This new knowledge can be helpful for further investigations on Ru-doped NIB cathodes, thus boosting their application in high-performing efficient devices with enhanced reversible capacity.

STRUCTURAL MODELS AND COMPUTATIONAL DETAILS

Spin-polarized density functional theory (DFT) calculations are performed within the DFT + U Hubbard-like correction scheme to overcome the large self-interaction error (SIE) that affects DFT when applied to mid-to-late first-row TM oxides with tightly localized d electrons.[41−43] Projector-augmented wave (PAW) potentials (Na_pv [Be]$2p^6 3s^1$; Ru [Kr]$4d^8$; Ni [Ar]$3d^{10}$; Mn [Ar]$3d^7$; O [He]$2s^2 2p^4$) and plane wave (PW) basis sets are used, as implemented in the Vienna ab-initio simulation package (VASP) code (version 5.4.4).[44−46] From electronic structure calculations, the net magnetic moment on each atom is derived as an estimation based on the computed spin density, that is, the difference in the up and down spin channels integrated within a sphere with a Wigner-Seitz radius for each atom type. We employ the Perdew−Burke−Ernzerhof (PBE) exchange−correlation functional within the generalized gradient approximation (GGA).[47] The on-site correction is applied to the d electrons of Ru, Ni, and Mn atoms with a unified average effective U-J parameter, U_{eff}, equal to 4 eV, as already successfully applied to TM oxides.[38,48−51] This choice is based on previous experience on mixed TM oxides where having the same average U_{eff} value for different TM oxides allowed us to obtain qualitatively reliable results.[52−54] The proposed approach has also been validated against hybrid HF-DFT calculations for the undoped parent material $Na_{0.75}Ni_{1/4}Mn_{3/4}O_2$.[28] The D3 dispersion correction with the Becke−Johnson (BJ) damping function is included to account for van der Waals (vdW) forces that represent dominant interactions in interfaces and layered materials.[55−58] A kinetic energy of 750 eV and a Γ-centered 4 × 4 × 4 *k*-point sampling mesh are used to ensure converged energies within 3 meV/f.u. with respect to the PW basis set size and Brillouin zone sampling, respectively. For all the calculations, the convergence threshold for energy is set to 10^{-5} eV. We build up a 4 × 4 × 1 supercell of $Na_{3/4}Ru_{1/8}Ni_{1/8}Mn_{3/4}O_2$ (i.e., stoichiometric NRNMO) containing 120 atoms within the $P6_3/mmc$ space group (and then 112 atoms for x_{Na} = 0.50 and 104 atoms for x_{Na} = 0.25). The TM disorder at the 2a atomic site can be simulated via the special quasi-random structure (SQS) approach as implemented in the Alloy Theoretic Automated Toolkit (ATAT) code.[59−61] The SQS is a state-of-the-art method to study solid solutions with two or more components and allows our models to properly account for the configurational entropy by achieving a mixed Ru/Ni/Mn occupancy. Na atoms are placed at edge and face sites according to the occupancy ratio reported in the literature.[40] Lattice constants and atomic positions for the $Na_xRu_{1/8}Ni_{1/8}Mn_{3/4}O_2$ system with x = 0.75, 0.50, and 0.25 are fully relaxed until the maximum forces acting on each atom are below 0.03 eV/Å. We introduce two Mn vacancies in the most homogeneous configuration to model the Mn-deficient $Na_xRu_{1/8}Ni_{1/8}Mn_{3/4-y}O_2$ (i.e., Mn-deficient NRNMO, y = 6.25%) systems and perform further relaxation of atomic positions with the same convergence criteria (see Figure S1 in Supporting Information for the structural model). No local aggregation of Mn vacancies has been reported in experiments, and macroscopic samples present isotropic properties, so we consider the homogeneous configuration as the best reliable model of the system.[32] To model O-defective structures, we remove one oxygen atom from the 4 × 4 × 1 supercell ($Na_xRu_{1/8}Ni_{1/8}Mn_{3/4-y}O_{2-\delta}$, V_O concentration δ = 1.56%). The same computational protocol described so far is applied for all the electronic structure calculations and geometry optimizations of O-defective structures and dioxygen complexes.

RESULTS AND DISCUSSION

The minimum-energy structures of $Na_xRu_{1/8}Ni_{1/8}Mn_{3/4}O_2$, with x = 0.75, 0.50, and 0.25, have been derived by means of the PBE + U(-D3BJ) approach. The computed lattice constants are shown in Table S1 of Supporting Information in comparison with experimental data. We obtain a 1.13% deviation on the a/b parameters and a 2.13% deviation on the c one, which is in the range of common errors from DFT calculations. Our structural models rely on the energy stability ensured by the SQS approach, which is the method of choice to properly account for configurational entropy in local minimum-energy structures.[59] Further investigation of the dynamic stability of these phases was beyond the aim of this work, where we can validate our structural model by direct comparison to experimental data.[40] However, it is worth mentioning that including phonon density calculations may improve the model description in the future. As a matter of fact, very little is known about the structure and electrochemistry of these kinds of electrodes in the high-voltage range, and even lower Na compositions (e.g.,x_{Na} < 0.25) result tricky to model and predict.[40] Since we can assume the lattice parameters to be constant upon introduction of Mn vacancies, the Mn-deficient NRNMO has been relaxed only in terms of atomic positions. A typical NIB operates by shuttling x Na^+ between the cathode and anode upon cycling; thus, the simplified cathode reaction at NRNMO can be written as

$$Na_{x_1}\text{RNMO} + (x_2 - x_1)Na^+ + (x_2 - x_1)e^- \rightleftharpoons Na_{x_2}\text{RNMO} \quad (1)$$

where Na_{x_1}RNMO and Na_{x_2}RNMO indicate the cathode stoichiometry, respectively, before and after the intercalation of $(x_2 - x_1)$ Na^+, which is the reduction process taking place at the cathode side upon charging. Defined this way, it is possible to consider an intercalation potential, V

$$V = -\frac{E_{Na_{x_2}\text{RNMO}} - E_{Na_{x_1}\text{RNMO}} - (x_2 - x_1)\frac{1}{2}E_{Na}}{(x_2 - x_1)} \quad (2)$$

where $E_{Na_{x_1}\text{RNMO}}$ and $E_{Na_{x_2}\text{RNMO}}$ are the total energies of the NRNMO material at x_1 and x_2 Na contents, as obtained within our computational protocol. The sodium metal (two-atoms containing bcc cell) is generally used as a reference, and thus, the $1/2E_{Na}$ will take into account the energy contribution from intercalating $(x_2 - x_1)$ Na atoms. To the best of our knowledge, this represents a common approach in the available

https://doi.org/10.1021/acsaem.2c01455
ACS Appl. Energy Mater. 2022, 5, 10721−10730

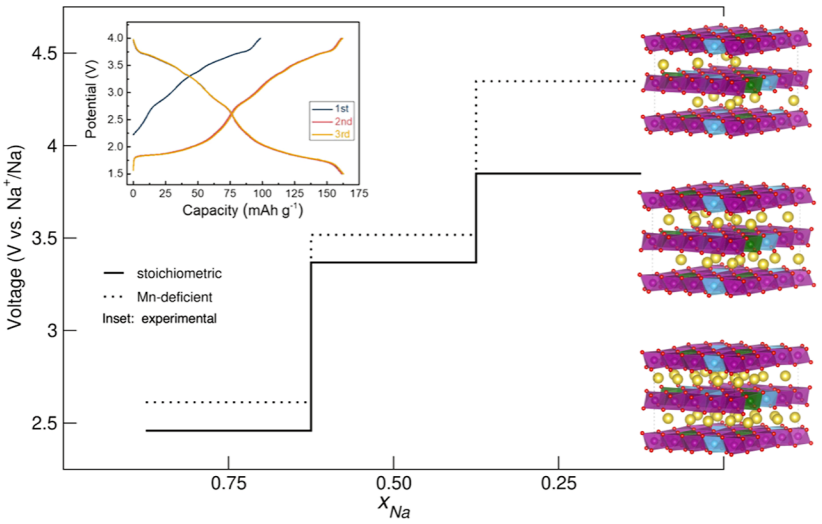

Figure 1. Sodium intercalation potential computed according to eq 2 at PBE + U(-D3BJ) for stoichiometric (solid line) and Mn-deficient (dashed line) NRNMO and plotted as a function of Na content. Inset: voltage-capacity profile of the P2-type $Na_{3/4}Ni_{1/3}Ru_{1/6}Mn_{1/2}O_2$ electrode from previous experimental data.[40] Reproduced from [Wang, Q. et al. ACS Appl. Mater. Interfaces 2020, 12 (35), 39056−39062]. Copyright 2020 American Chemical Society. The corresponding minimum-energy structures are displayed on the right side of the plot. Color code: Na, yellow; Ru, blue; Ni, green; Mn, violet; and O, red; TMO_6 octahedra are depicted in the corresponding colors.

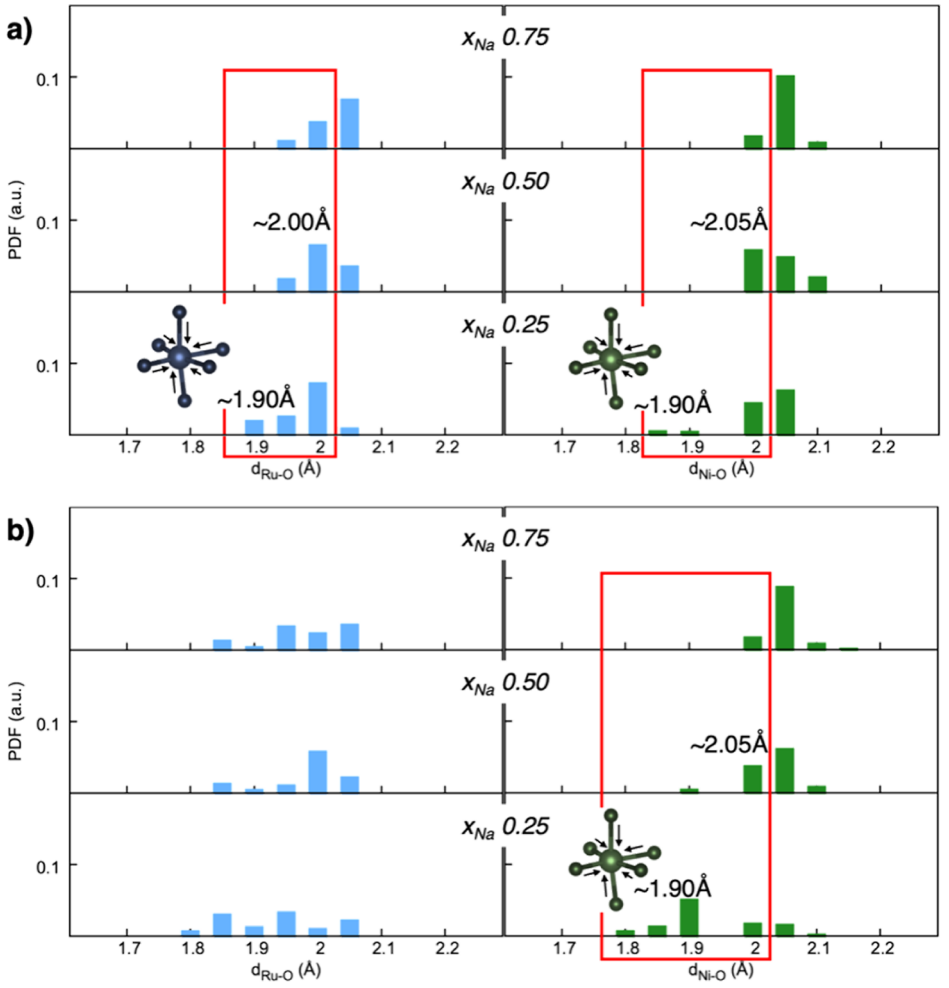

Figure 2. Pair distribution functions (PDF) of Ru−O (blue) and Ni−O (green) distances in (a) stoichiometric and (b) Mn-deficient NRNMO computed at PBE + U(-D3BJ).

literature to calculate a theoretical voltage-capacity profile for electrode materials.[7] Figure 1 shows the resulting intercalation potential as a function of the Na load and provides a direct comparison with the experimental voltage-capacity plot in the

https://doi.org/10.1021/acsaem.2c01455
ACS Appl. Energy Mater. 2022, 5, 10721−10730

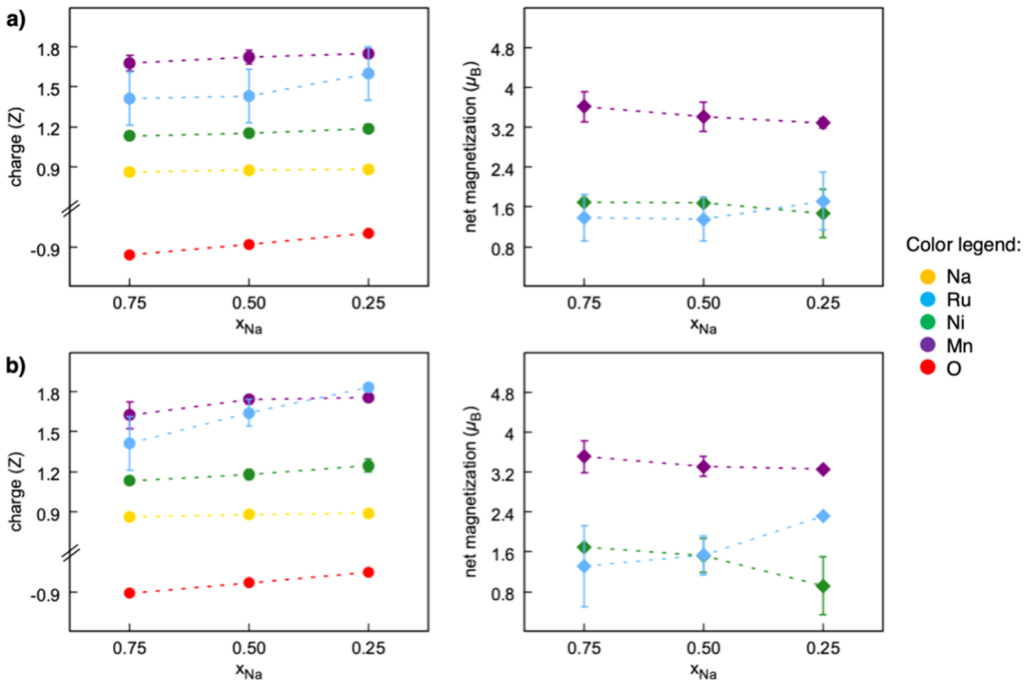

Figure 3. Average Bader charges and net magnetization computed for each element sublattice at PBE + U(-D3BJ) in (a) stoichiometric and (b) Mn-deficient NRNMO as a function of Na content. Standard deviations are displayed as error bars at each point. Color code: Na, yellow; Ru, blue; Ni, green; Mn, violet; and O, red.

inset.[40] The smooth profile obtained from experiments suggests good structural retention upon electrode charge, which in turn validates our P2 model (reported on the right side of Figure 1) within the explored voltage range. We can clearly see that p-type doping induced by Mn deficiency shifts the intercalation potential at higher values, the increase being more evident at a high state of charge. As far as we know, the introduction of TM vacancies does represent a possible strategy toward higher energy NIB cathodes[32] that we have also addressed in our previous work from the theoretical point of view.[28,29] However, it is important to assess to what extent the presence of Mn-vacant sites and the following increased working potential can affect the charge compensation mechanisms upon desodiation of Ru-doped layered oxides, that is, the anionic redox chemistry and the underlying reversibility.

The structural evolution of NRNMO, in both stoichiometric and Mn-deficient forms, is analyzed by means of pair distribution functions (PDFs) for TM-O distances (reported in Figures 2 and S2). The short-range peaks and the related shifts upon desodiation can account for bond distortion within the TMO_6 octahedra: the Mn−O distances are mostly kept constant at decreasing Na content (see Figure S2 in Supporting Information); Ru-centered octahedra show bond compression from ∼2.00 to ∼1.90 Å at x_{Na} = 0.25 in the stoichiometric NRNMO, while in the Mn-deficient phase Ru−O distances cover a wide range of values at each sodiation degree (see blue histogram in the left panels of Figure 2a,b); Ni−O bonds undergo shortening from ∼2.05 to ∼1.90 Å at x_{Na} = 0.25, especially in Mn-deficient NRNMO (green histogram in the right panels of Figure 2a,b). The pictorial representations and red boxes in Figure 2 highlight this effect. The correlation between the TMO_6 octahedra distortion and TM oxidation change is well established in the literature.[28,62] Thus, the wide range of distance spanned by Ru−O bonds may be ascribed to the coexistence of differently charged Ru atoms and the partial oxidation occurring at low Na content of stoichiometric NRNMO, as well as the compression effect in the NiO_6 octahedra may be due to a change in Ni oxidation states occurring along Na^+ removal. The analysis of electronic properties can shed light on this correlation.

Calculation of average charges for each element sublattice reveals that TM-O bonds in both stoichiometric and Mn-deficient NRNMO are highly covalent, as suggested by the Bader charge values far below the ionic limits (left panels in Figure 3a,b), as well as by the hybridization of TM d and O p states that can be observed in the projected density of states (PDOS) in Figure S3. It is worth mentioning that the average charge on oxygen sublattice undergoes a slight increase, for example, less negative values, when going from x_{Na} = 0.75 to 0.25 (red lines in Figure 3a,b), which may suggest the activation of anionic redox at a high voltage. The fairly constant trend in TM charges upon desodiation is ascribed to the so-called negative-feedback charge regulation mechanism: the new bonding orbitals formed in TM-O bonds upon electron gain will be shifted toward the ligand due to realignment of energy levels, and this leads to depopulation of TM charges in the bonding states, with the charge allocated at the TM site remaining approximately constant.[63] Indeed, the variation of Mn and Ni oxidation states upon desodiation can be more easily evinced by the magnetization trends (right panels in Figure 3a,b): (i) both stoichiometric and Mn-deficient NRNMO feature a mixed oxidation within the Mn sublattice (∼3.5 μ_B—d^4/d^3 configuration), meaning that both Mn^{3+} and Mn^{4+} states are present (violet lines); (ii) the average Ni magnetization only slightly decreases upon desodiation in the stoichiometric form while shifting down to ∼0.8 μ_B at x_{Na} = 0.25 in Mn-deficient NRNMO and indicating the $Ni^{2+} \rightarrow Ni^{3+}$ oxidation (d^7 low-spin configuration, see green lines). For what concerns Ru in

https://doi.org/10.1021/acsaem.2c01455
ACS Appl. Energy Mater. 2022, 5, 10721−10730

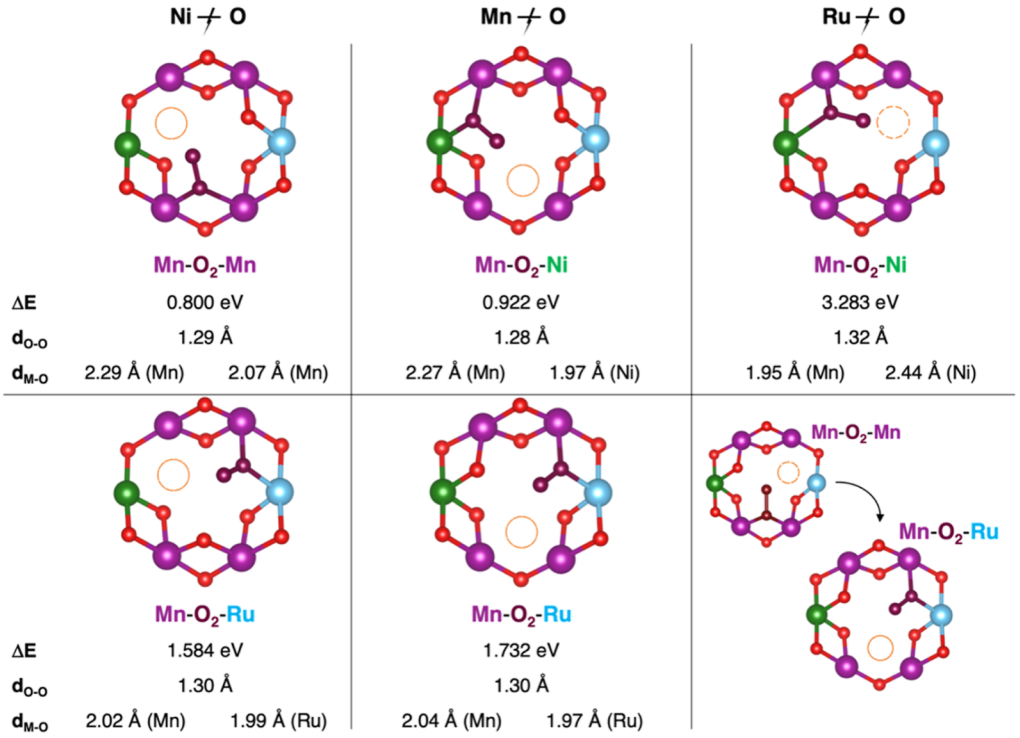

Figure 4. Formation of a dioxygen-metal complex in $Na_{1/4}Ru_{1/8}Ni_{1/8}Mn_{3/4-y}O_2$ at the Mn deficiency site. Color code as in Figure 1, O (dioxygen), brown. The orange circles highlight the original position before dioxygen formation. Only atoms around the dioxygen species are shown for clarity. Corresponding formation energy, ΔE, computed according to eq 3 at PBE + U(-D3BJ) and structural details (d_{O-O} and d_{M-O} distances) are also reported.

stoichiometric NRNMO, both charge and magnetization increase at x_{Na} = 0.25 (blue lines in Figure 3a), suggesting a partial variation from the mixed Ru^{3+}/Ru^{4+} oxidation state (~1.5 μ_B—d^5/d^4 low-spin configuration) in agreement with the literature.[40] On the other hand, a more significant change is predicted in the Mn-deficient structure, where the Ru sublattice is oxidized to Ru^{5+} (~2.4 μ_B—d^3 configuration, see blue lines in Figure 3b). Other quantum mechanics methods for more accurate calculation of oxidation states have been developed.[64] The use of more effective approaches aiming to decouple the contribution of TM-ligand orbital mixing from the actual occupation of the TM d orbitals will certainly improve the electronic structure analysis and can be addressed in the future. Indeed, our evaluation of TM oxidation state variation upon desodiation remains qualitative, with the net magnetization results showing good agreement with available experimental data.[40]

These findings show that the desodiation process strongly affects the electronic structure of the NRNMO material and directly involves Ni and Ru sublattices. As suggested by the charge increasing trend on the O sublattice, we investigate to what extent its oxidation degree would be beneficial for the cathode performance. The same method adopted and validated in our former work on $Na_xNi_{0.25}Mn_{0.68}O_2$ and the Fe-doped counterpart (NNMO and NFNMO, respectively) is applied here to address the O^{2-} evolution in NRNMO.[28,29] As anticipated in the introduction, the Mn-deficient NRNMO can be considered as the initial structure along the oxide-to-superoxide process, that is, the formation of dioxygen complexes coordinated to TM atoms near the Mn vacancy site as a reasonable consequence of O^{2-} oxidation at x_{Na} = 0.25. These latter structures are formed within the lattice via the displacement of two oxygen atoms from their regular positions to certain intermediated coordinates. The associated energy variation can be defined as:

$$\Delta E = E_{TM-O_2-TM} - E_{Na_{0.25}Ru_{1/8}Ni_{1/8}Mn_{3/4-y}O_2} \quad (3)$$

where E_{TM-O_2-TM} is the total energy of the dioxygen-metal complex (TM−O_2−TM, see Figure 4 and related discussion further in the text) formed in a specific configuration and $E_{Na_{0.25}Ru_{1/8}Ni_{1/8}Mn_{3/4-y}O_2}$ is the total energy of the Mn-deficient NRNMO used as a reference. We consider all possible chemical environments that differ for the position of both binding and leaving oxygen. In this way, we can dissect the role of each TM dopant in the dioxygen formation process. As clarified in Figure 4, the following configurations are explored (from left to right): (i) Mn−O_2−Mn and Mn−O_2−Ru, as a result of Ni−O bond breaking; (ii) Mn−O_2−Ni and Mn−O_2−Ru originated from the breaking of the Mn−O bond; and (iii) Mn−O_2−Ni and Mn−O_2−Mn coupled to Ru−O breaking. For each configuration, the PBE + U(-D3BJ) minimum-energy structure consists of superoxide moieties binding the TM atoms in a bridging coordination mode, as suggested by the O−O bond length ranging from 1.28 to 1.32 Å and the pair of TM-O distance lying between 1.95 and 2.44 Å.[65,66] In all the explored configurations, the dioxygen moiety is found to bind the nearby transition metals in different coordination modes. Indeed, no free O_2 is detected, contrary to what was previously observed for the undoped $Na_xNi_{0.25}Mn_{0.68}O_2$.[28] The formation of such dioxygen-metal complexes can unveil the oxygen redox mechanism occurring in NRNMO at a high voltage: it represents the oxide-to-superoxide transition, which relies on the partial oxidation of the oxide sublattice and thus accounts for the anionic redox chemistry. As first observed exper-

https://doi.org/10.1021/acsaem.2c01455
ACS Appl. Energy Mater. 2022, 5, 10721−10730

imentally and now proved theoretically,[40] the Ru-doped material does not fully exert the anionic redox since further oxidation to O_2 is inhibited and the cathode can work in reversible conditions. By looking at the calculated energy values, we can carry out a comparative analysis aiming to identify to what extent the chemical environment can alter the dioxygen-metal formation mechanism. It is evident that both binding and breaking sites affect the associated energetics: the most favorable cases are found when only Ni and Mn atoms are involved, leading to Mn−O_2−Mn and Mn−O_2−Ni species via preferential breaking of Ni- and Mn−O bonds (ΔE = 0.800 and 0.922 eV, respectively). In fact, much higher energy is required to form the dioxygen in an Mn−O_2−Ru configuration when coupled to the same Ni-/Mn−O bond breaking (ΔE = 1.584 and 1.732 eV). Although binding to Ru leads to less stable dioxygen compounds, the formation mechanism is even more unlikely to occur via breaking of Ru−O bonds: the high-energy Mn−O_2−Ni configuration can be formed with ΔE = 3.283 eV, while the Mn−O_2−Mn does not even represent a stable structure and dioxygen moves toward the Ru site to restore the strong Ru−O bond (leading to the same Mn−O_2−Ru structure with ΔE = 1.732 eV). The so-obtained formation energies are higher than the ones calculated in NNMO and NFNMO,[28,29] this outcome being comparable to the higher dimerization barriers reported by the Shao-Horn group.[38] Despite being large and positive, these values imply that non-spontaneous processes can still be accessible under NIB operating conditions, that is, upon charge. However, we should warn the reader that they need to be interpreted only comparatively, as the absolute numbers can sensibly vary by considering the conversion to free energy variations via phonon calculations as well as the effects of an electrolyte or an external electric field. Herein, our purpose is to provide the simplest model that is able to explain the oxygen redox activity and the underlying mechanisms observed in the experiments.

The intense debate in the literature on activation and control of O-based redox in layered Na_xTMO_2 seems to agree in identifying the TM−O bond strength as a key factor which tuning strategies may be referred to. To this end, we have previously shown that this property can be easily quantified in terms of oxygen vacancy formation energies:[28,29] the lower the formation energy of a given oxygen vacancy, the easier the tendency to break the involved chemical bonds. To the best of our knowledge, investigating oxygen vacancy formation represents a suitable way in materials science to address open questions about defect chemistry in simple and mixed transition metal oxides or oxide migration in perovskite structures.[67−69] In the case of a layered oxide with the general formula Na_xTMO_2, the reaction leading to the oxygen defective material can be written as

$$Na_xTMO_2 \rightarrow Na_xTMO_2^* + \frac{1}{2}O_2 \quad (4)$$

where Na_xTMO_2 and $Na_xTMO_2{}^*$ are, respectively, the layered oxide in its pristine structure and the corresponding defective system after formation of the oxygen vacancy, V_O. The removal of one oxygen atom from our 4 × 4 × 1 supercell of $Na_xRu_{1/8}Ni_{1/8}Mn_{3/4-y}O_2$ system corresponds to a 1.56% oxygen vacancy concentration. The free oxygen molecule in its triplet state is usually considered as reference.[67−69] The associated energy variation can be calculated according to eq 5

$$E_{V_O} = E_{Na_{0.25}Ru_{1/8}Ni_{1/8}Mn_{3/4-y}O_2{}^*} - E_{Na_{0.25}Ru_{1/8}Ni_{1/8}Mn_{3/4-y}O_2} + \frac{1}{2}E_{O_2} \quad (5)$$

where $E_{Na_{0.25}Ru_{1/8}Ni_{1/8}Mn_{3/4-y}O_2{}^*}$ and $E_{Na_{0.25}Ru_{1/8}Ni_{1/8}Mn_{3/4-y}O_2}$ are the total energies of the oxygen defective and the pristine $Na_xRu_{1/8}Ni_{1/8}Mn_{3/4-y}O_2$, respectively, and E_{O_2} is the total energy of the oxygen molecule as computed in its triplet ground state at the same level of theory. We consider different kinds of oxygen vacancies, differing for both the coordination (twofold and threefold coordinated, $V_O(2c)$ and $V_O(3c)$, respectively) and the chemical environment (according to the coordinating atoms: Mn, Mn/Ni, Mn/Ru, and Mn/Ni/Ru, see Figure S4 in Supporting Information for further details on the labeling). Table 1 shows the results for $V_O(2c)$, while E_{V_O} for three-coordinated vacancies are collected in Table S2. By comparing the $V_O(2c)$ values obtained here for NRNMO to our former results on Fe-doped and undoped NNMO (see the corresponding rows in Table 1), we can see that the E_{V_O} trend is altered: besides the Mn/Ni configuration showing the lowest E_{V_O} values in all materials, the effect of Ru doping is the opposite compared to Fe, leading to E_{V_O}(Mn/Ru) > E_{V_O}(Mn). While Fe doping was introducing mild TM−O covalency conditions, the introduction of Ru atoms results in a significant strengthening of the chemical bond. It is worth noticing that the doping effects on the $V_O(3c)$ are more intertwined: removal of oxygen atom is found to be more difficult not only from Ru- but also from Ni-containing configurations (E_{V_O}(Mn/Ru, Mn/Ni) > E_{V_O}(Mn)). In the case of the most heterogeneous sites (i.e., Mn/Ni/Ru), Ru and Ni seem to play a synergic effect that still leads to a higher E_{V_O} compared to E_{V_O}(Mn) (see Table S2 in Supporting Information). Conversely, the E_{V_O} for Mn/Fe and Mn/Ni/Fe in NFNMO were always lower than Mn and Mn/Ni ones, suggesting that the opposite effect of Ru doping compared to Fe is even exerted in the stabilization of the oxide moiety in a Ni-containing site.

Table 1. Formation Energies of Twofold-Coordinated Oxygen Vacancies, $E_{V_O(2c)}$ (eV), Computed in Different Chemical Environments (Mn, Mn/Ni, and Mn/Ru, See Figure S4 in Supporting Information) at PBE + U(-D3BJ) According to eq 5[a]

	Mn	Mn/Ni	Mn/Ru	Mn/Fe
NRNMO (this work)	1.404	1.101	2.498	
NFNMO[29]	1.587	1.152		1.397
NNMO[28]	1.515	1.079		

[a]Mn/Fe configurations from NFNMO and other previous results obtained in NNMO with the same method are also reported for direct comparison.[28,29]

From the values shown in Table 1 and the discussion reported so far, it is clear that the V_O formation energy trend directly reflects the tendency of a given composition to release an oxygen atom and thus can represent a solid way to predict different activities toward the $O^{2-}/O^-/O_2$ evolution from predictions of TM−O bond strength. We can conclude that Ru doping would ensure such desirable strong TM−O bonds for preventing irreversible O_2 loss and allowing efficient reversible conditions at a high working voltage.

https://doi.org/10.1021/acsaem.2c01455
ACS Appl. Energy Mater. 2022, 5, 10721−10730

CONCLUSIONS AND OUTLOOK

In this work, we have presented the theoretical characterization of a Ru-doped Na_xTMO_2 (TM = Ru, Ni, and Mn) system with promising properties for application as a cathode material in Na-ion batteries. The structural evolution and electronic features in $Na_xRu_{1/8}Ni_{1/8}Mn_{3/4}O_2$ have been derived from PBE + U(-D3BJ) calculations as a function of Na content to simulate the cathode charging process. We have also modeled the Mn-deficient counterpart (e.g., $Na_xRu_{1/8}Ni_{1/8}Mn_{3/4-y}O_2$) in order to provide insightful design strategies for high-energy cathodes and explore the mechanism of O^{2-}/O^{-} evolution. With the computational method being validated according to the existent experimental data and former ab initio simulations on similar materials, we can sum up our results as follows:

- Mn sublattice retains its mixed Mn^{3+}/Mn^{4+} oxidation upon desodiation as suggested by constant charge/magnetization and steady PDF of Mn−O distances in both stoichiometric and Mn-deficient NRNMO;
- Ni^{2+} undergoes oxidation to Ni^{3+} at low Na content, leading to bond shrinking within the Ni-centered octahedra, the effect being more remarkable in the Mn-deficient form;
- the mixed Ru^{3+}/Ru^{4+} seems to be involved in the charge compensation at x_{Na} = 0.25 of both stoichiometric and Mn-deficient NRNMO, with a net oxidation up to Ru^{5+} occurring in the latter, also coupled to Ru−O bond compression;
- two low-energy superoxide species can be formed at x_{Na} = 0.25 near the Mn deficiency site via preferential breaking of Ni- and Mn−O bonds, featuring a bridging coordination mode to Mn/Mn and Mn/Ni atoms (Mn−O_2−Mn and Mn−O_2−Ni, respectively). The more labile character of Ni- and Mn−O is confirmed by lower V_O formation energies;
- dioxygen formation via Ru−O breaking is more unlikely to occur due to the enhanced bond strength, also quantified in terms of $E(V_O)$.

Thanks to the broad and inspiring literature on Li-ion analogues, despite being few, the experimental efforts to exploit highly covalent transition metal oxides in efficient NIB devices are well underway. All-in-all, these findings shed light on the charge compensation occurring at high voltage in the P2-type Na_xTMO_2 (TM = Ru, Ni, and Mn) layered oxide that is described with atomistic detail. By decoupling the single element contributions, we could highlight the key role exerted by the Ru dopant in stabilizing the oxide lattice redox and thus promoting access to reversible anionic chemistry. This study paves the route for future investigation, aiming to consider the interplay of other charge compensation mechanisms that may hamper the cathode capacity, for example, TM/oxygen vacancies and antisite defects at different desodiation degrees. Great steps forward in the design of highly performing cathode materials are being made and, as has been demonstrated here, the theoretical intake can sensibly help to boost their future deployment in effective NIB devices.

ASSOCIATED CONTENT

Supporting Information

The Supporting Information is available free of charge at https://pubs.acs.org/doi/10.1021/acsaem.2c01455.

Computed lattice parameters at different sodium contents; structural models for Mn-deficient NRNMO; Mn−O PDFs; projected density of states (PDOS) for stoichiometric and Mn-deficient NRNMO; structural details of O-defective structures; and formation energies for V_O(3c) (PDF)

AUTHOR INFORMATION

Corresponding Authors

Ana B. Muñoz-García − *National Reference Center for Electrochemical Energy Storage (GISEL)-INSTM, 50121 Florence, Italy; Department of Physics "Ettore Pancini", University of Naples Federico II, Comp. Univ. Monte S. Angelo, 80126 Naples, Italy;* orcid.org/0000-0002-9940-7358; Email: anabelen.munozgarcia@unina.it

Michele Pavone − *Department of Chemical Sciences, University of Naples Federico II, Comp. Univ. Monte S. Angelo, 80126 Naples, Italy; National Reference Center for Electrochemical Energy Storage (GISEL)-INSTM, 50121 Florence, Italy;* orcid.org/0000-0001-7549-631X; Email: michele.pavone@unina.it

Authors

Arianna Massaro − *Department of Chemical Sciences, University of Naples Federico II, Comp. Univ. Monte S. Angelo, 80126 Naples, Italy; National Reference Center for Electrochemical Energy Storage (GISEL)-INSTM, 50121 Florence, Italy;* orcid.org/0000-0003-2950-6745

Aniello Langella − *Department of Chemical Sciences, University of Naples Federico II, Comp. Univ. Monte S. Angelo, 80126 Naples, Italy*

Claudio Gerbaldi − *National Reference Center for Electrochemical Energy Storage (GISEL)-INSTM, 50121 Florence, Italy; GAME Lab, Department of Applied Science and Technology (DISAT), Politecnico di Torino, 10129 Torino, Italy;* orcid.org/0000-0002-8084-0143

Giuseppe Antonio Elia − *National Reference Center for Electrochemical Energy Storage (GISEL)-INSTM, 50121 Florence, Italy; GAME Lab, Department of Applied Science and Technology (DISAT), Politecnico di Torino, 10129 Torino, Italy;* orcid.org/0000-0001-6790-1143

Complete contact information is available at: https://pubs.acs.org/10.1021/acsaem.2c01455

Notes

The authors declare no competing financial interest.

ACKNOWLEDGMENTS

The computing resources and the related technical support used for this work have been provided by CRESCO/ENEAGRID High Performance Computing infrastructure and its staff.[70] CRESCO/ENEAGRID High Performance Computing infrastructure is funded by ENEA, Italy, the Italian National Agency for New Technologies, Energy and Sustainable Economic Development and by Italian and European research programs; see https://www.cresco.enea.it for information.

REFERENCES

(1) Dunn, B.; Kamath, H.; Tarascon, J.-M. Electrical Energy Storage for the Grid: A Battery of Choices. *Science* **2011**, *334*, 928−935.

(2) Larcher, D.; Tarascon, J. M. Towards Greener and More Sustainable Batteries for Electrical Energy Storage. *Nat. Chem.* **2015**, *7*, 19−29.

(3) Ferrari, S.; Falco, M.; Muñoz-García, A. B.; Bonomo, M.; Brutti, S.; Pavone, M.; Gerbaldi, C. Solid-State Post Li Metal Ion Batteries: A

Sustainable Forthcoming Reality? *Adv. Energy Mater.* **2021**, *11*, 2100785.
(4) Eftekhari, A.; Kim, D.-W. Sodium-Ion Batteries: New Opportunities beyond Energy Storage by Lithium. *J. Power Sources* **2018**, *395*, 336−348.
(5) Armand, M.; Axmann, P.; Bresser, D.; Copley, M.; Edström, K.; Ekberg, C.; Guyomard, D.; Lestriez, B.; Novák, P.; Petranikova, M.; Porcher, W.; Trabesinger, S.; Wohlfahrt-Mehrens, M.; Zhang, H. Lithium-Ion Batteries − Current State of the Art and Anticipated Developments. *J. Power Sources* **2020**, *479*, 228708.
(6) Wang, L. P.; Yu, L.; Wang, M.; Srinivasan, Z. J.; Xu, X. Recent Developments in Electrode Materials for Sodium-Ion Batteries. *J. Mater. Chem. A* **2015**, *3*, 9353−9378.
(7) Bai, Q.; Yang, L.; Chen, H.; Mo, Y. Computational Studies of Electrode Materials in Sodium-Ion Batteries. *Adv. Energy Mater.* **2018**, *8*, 1702998.
(8) Islam, M. S.; Fisher, C. A. J. Lithium and Sodium Battery Cathode Materials: Computational Insights into Voltage, Diffusion and Nanostructural Properties. *Chem. Soc. Rev.* **2014**, *43*, 185−204.
(9) Wang, S.; Qin, M.; Huang, M.; Huang, X.; Li, Q.; You, Y. Organic Solvothermal Method Promoted Monoclinic Prussian Blue as a Superior Cathode for Na-Ion Batteries. *ACS Appl. Energy Mater.* **2022**, *5*, 6927−6935.
(10) Zhang, L.; Yu, L.; Li, O. L.; Choi, S.-Y.; Saeed, G.; Lee, D.; Kim, K. H. Facile Synthesis of Necessary Amorphous Structure $FePO_4$ Nanospheres as Superior Sodium-Ion Battery Cathodes. *ACS Appl. Energy Mater.* **2022**, *5*, 5954−5963.
(11) Shi, H.; Li, J.; Liu, M.; Luo, A.; Li, L.; Luo, Z.; Wang, X. Multiple Strategies toward Advanced P2-Type Layered Na_xMnO_2 for Low-Cost Sodium-Ion Batteries. *ACS Appl. Energy Mater.* **2021**, *4*, 8183−8192.
(12) Zhao, C.; Yao, Z.; Wang, Q.; Li, H.; Wang, J.; Liu, M.; Ganapathy, S.; Lu, Y.; Cabana, J.; Li, B.; Bai, X.; Aspuru-Guzik, A.; Wagemaker, M.; Chen, L.; Hu, Y.-S. Revealing High Na-Content P2-Type Layered Oxides as Advanced Sodium-Ion Cathodes. *J. Am. Chem. Soc.* **2020**, *142*, 5742−5750.
(13) Delmas, C.; Fouassier, C.; Hagenmuller, P. Structural Classification and Properties of the Layered Oxides. *Phys. B+C* **1980**, *99*, 81−85.
(14) Clément, R. J.; Bruce, P. G.; Grey, C. P. Review—Manganese-Based P2-Type Transition Metal Oxides as Sodium-Ion Battery Cathode Materials. *J. Electrochem. Soc.* **2015**, *162*, A2589−A2604.
(15) Goodenough, J. B.; Kim, Y. Challenges for Rechargeable Li Batteries. *Chem. Mater.* **2010**, *22*, 587−603.
(16) Li, K.; Xue, D. Estimation of Electronegativity Values of Elements in Different Valence States. *J. Phys. Chem. A* **2006**, *110*, 11332−11337.
(17) Grimaud, A.; Hong, W. T.; Shao-Horn, Y.; Tarascon, J. M. Anionic Redox Processes for Electrochemical Devices. *Nat. Mater.* **2016**, *15*, 121−126.
(18) Assat, G.; Tarascon, J. M. Fundamental Understanding and Practical Challenges of Anionic Redox Activity in Li-Ion Batteries. *Nat. Energy* **2018**, *3*, 373−386.
(19) Wang, Q.; Mariyappan, S.; Rousse, G.; Morozov, A. V.; Porcheron, B.; Dedryvère, R.; Wu, J.; Yang, W.; Zhang, L.; Chakir, M.; Avdeev, M.; Deschamps, M.; Yu, Y.-S.; Cabana, J.; Doublet, M.-L.; Abakumov, A. M.; Tarascon, J.-M. Unlocking Anionic Redox Activity in O3-Type Sodium 3d Layered Oxides via Li Substitution. *Nat. Mater.* **2021**, *20*, 353.
(20) Ben Yahia, M.; Vergnet, J.; Saubanère, M.; Doublet, M.-L. Unified Picture of Anionic Redox in Li/Na-Ion Batteries. *Nat. Mater.* **2019**, *18*, 496−502.
(21) Li, Z.; Kong, W.; Yu, Y.; Zhang, J.; Wong, D.; Xu, Z.; Chen, Z.; Schulz, C.; Bartkowiak, M.; Liu, X. Tuning Bulk O_2 and Nonbonding Oxygen State for Reversible Anionic Redox Chemistry in P2-Layered Cathodes. *Angew. Chemie* **2022**, *134*, No. e202115552.
(22) Zhang, Y.; Wu, M.; Ma, J.; Wei, G.; Ling, Y.; Zhang, R.; Huang, Y. Revisiting the $Na_{2/3}Ni_{1/3}Mn_{2/3}O_2$ Cathode: Oxygen Redox Chemistry and Oxygen Release Suppression. *ACS Cent. Sci.* **2020**, *6*, 232−240.
(23) Ma, C.; Alvarado, J.; Xu, J.; Clément, R. J.; Kodur, M.; Tong, W.; Grey, C. P.; Meng, Y. S. Exploring Oxygen Activity in the High Energy P2-Type $Na_{0.78}Ni_{0.23}Mn_{0.69}O_2$ Cathode Material for Na-Ion Batteries. *J. Am. Chem. Soc.* **2017**, *139*, 4835−4845.
(24) Risthaus, T.; Zhou, D.; Cao, X.; He, X.; Qiu, B.; Wang, J.; Zhang, L.; Liu, Z.; Paillard, E.; Schumacher, G.; Winter, M.; Li, J. A High-Capacity P2 $Na_{2/3}Ni_{1/3}Mn_{2/3}O_2$ Cathode Material for Sodium Ion Batteries with Oxygen Activity. *J. Power Sources* **2018**, *395*, 16−24.
(25) Vergnet, J.; Saubanère, M.; Doublet, M.-L.; Tarascon, J.-M. The Structural Stability of P2-Layered Na-Based Electrodes during Anionic Redox. *Joule* **2020**, *4*, 420−434.
(26) Wang, Y.; Feng, Z.; Cui, P.; Zhu, W.; Gong, Y.; Girard, M.-A.; Lajoie, G.; Trottier, J.; Zhang, Q.; Gu, L.; Wang, Y.; Zuo, W.; Yang, Y.; Goodenough, J. B.; Zaghib, K. Pillar-Beam Structures Prevent Layered Cathode Materials from Destructive Phase Transitions. *Nat. Commun.* **2021**, *12*, 13.
(27) Wang, Q.-C.; Meng, J.-K.; Yue, X.-Y.; Qiu, Q.-Q.; Song, Y.; Wu, X.-J.; Fu, Z.-W.; Xia, Y.-Y.; Shadike, Z.; Wu, J.; Yang, X.-Q.; Zhou, Y.-N. Tuning P2-Structured Cathode Material by Na-Site Mg Substitution for Na-Ion Batteries. *J. Am. Chem. Soc.* **2019**, *141*, 840−848.
(28) Massaro, A.; Muñoz-García, A. B.; Prosini, P. P.; Gerbaldi, C.; Pavone, M. Unveiling Oxygen Redox Activity in P2-Type $Na_xNi_{0.25}Mn_{0.68}O_2$ High-Energy Cathode for Na-Ion Batteries. *ACS Energy Lett.* **2021**, *6*, 2470−2480.
(29) Massaro, A.; Langella, A.; Muñoz-García, A. B.; Pavone, M. First-principles Insights on Anion Redox Activity in $Na_xFe_{1/8}Ni_{1/8}Mn_{3/4}O_2$: Toward Efficient High-energy Cathodes for Na-ion Batteries. *J. Am. Ceram. Soc.* **2022**, *334*, 1−11, DOI: 10.1111/jace.18494.
(30) Yu, C.-J.; Pak, Y.-C.; Kim, C.-H.; Kim, J.-S.; Ri, K.-C.; Ri, K.-H.; Choe, S.-H.; Cottenier, S. Structural and Electrochemical Trends in Mixed Manganese Oxides Na_xMO_2 (M = Mn, Fe, Co, Ni) for Sodium-Ion Battery Cathode. *J. Power Sources* **2021**, *511*, 230395.
(31) Zhao, C.; Yao, Z.; Wang, J.; Lu, Y.; Bai, X.; Aspuru-Guzik, A.; Chen, L.; Hu, Y.-S. Ti Substitution Facilitating Oxygen Oxidation in $Na_{2/3}Mg_{1/3}Ti_{1/6}Mn_{1/2}O_2$ Cathode. *Chem* **2019**, *5*, 2913−2925.
(32) Shen, Q.; Liu, Y.; Zhao, X.; Jin, J.; Wang, Y.; Li, S.; Li, P.; Qu, X.; Jiao, L. Transition-Metal Vacancy Manufacturing and Sodium-Site Doping Enable a High-Performance Layered Oxide Cathode through Cationic and Anionic Redox Chemistry. *Adv. Funct. Mater.* **2021**, *31*, 2106923.
(33) Mortemard de Boisse, B.; Nishimura, S.; Watanabe, E.; Lander, L.; Tsuchimoto, A.; Kikkawa, J.; Kobayashi, E.; Asakura, D.; Okubo, M.; Yamada, A. Highly Reversible Oxygen-Redox Chemistry at 4.1 V in $Na_{4/7-x}[\square_{1/7}Mn_{6/7}]O_2$ (□: Mn Vacancy). *Adv. Energy Mater* **2018**, *8*, 1800409.
(34) Saubanère, M.; McCalla, E.; Tarascon, J. M.; Doublet, M. L. The Intriguing Question of Anionic Redox in High-Energy Density Cathodes for Li-Ion Batteries. *Energy Environ. Sci.* **2016**, *9*, 984−991.
(35) Muy, S.; Bachman, J. C.; Giordano, L.; Chang, H. H.; Abernathy, D. L.; Bansal, D.; Delaire, O.; Hori, S.; Kanno, R.; Maglia, F.; Lupart, S.; Lamp, P.; Shao-Horn, Y. Tuning Mobility and Stability of Lithium Ion Conductors Based on Lattice Dynamics. *Energy Environ. Sci.* **2018**, *11*, 850−859.
(36) Yu, Y.; Karayaylali, P.; Nowak, S. H.; Giordano, L.; Gauthier, M.; Hong, W.; Kou, R.; Li, Q.; Vinson, J.; Kroll, T.; Sokaras, D.; Sun, C. J.; Charles, N.; Maglia, F.; Jung, R.; Shao-Horn, Y. Revealing Electronic Signatures of Lattice Oxygen Redox in Lithium Ruthenates and Implications for High-Energy Li-Ion Battery Material Designs. *Chem. Mater.* **2019**, *31*, 7864−7876.
(37) Charles, N.; Yu, Y.; Giordano, L.; Jung, R.; Maglia, F.; Shao-Horn, Y. Toward Establishing Electronic and Phononic Signatures of Reversible Lattice Oxygen Oxidation in Lithium Transition Metal Oxides For Li-Ion Batteries. *Chem. Mater.* **2020**, *32*, 5502−5514.

(38) Yu, Y.; Karayaylali, P.; Sokaras, D.; Giordano, L.; Kou, R.; Sun, C.-J.; Maglia, F.; Jung, R.; Gittleson, F. S.; Shao-Horn, Y. Towards Controlling the Reversibility of Anionic Redox in Transition Metal Oxides for High-Energy Li-Ion Positive Electrodes. *Energy Environ. Sci.* **2021**, *14*, 2322−2334.
(39) Kiziltas-Yavuz, N.; Bhaskar, A.; Dixon, D.; Yavuz, M.; Nikolowski, K.; Lu, L.; Eichel, R.-A.; Ehrenberg, H. Improving the Rate Capability of High Voltage Lithium-Ion Battery Cathode Material $LiNi_{0.5}Mn_{1.5}O_4$ by Ruthenium Doping. *J. Power Sources* **2014**, *267*, 533−541.
(40) Wang, Q.; Jiang, K.; Feng, Y.; Chu, S.; Zhang, X.; Wang, P.; Guo, S.; Zhou, H. P2-Type Layered $Na_{0.75}Ni_{1/3}Ru_{1/6}Mn_{1/2}O_2$ Cathode Material with Excellent Rate Performance for Sodium-Ion Batteries. *ACS Appl. Mater. Interfaces* **2020**, *12*, 39056−39062.
(41) Hohenberg, P.; Kohn, W. Inhomogeneous Electron Gas. *Phys. Rev.* **1964**, *136*, B864−B871.
(42) Kohn, W.; Sham, L. J. Self-Consistent Equations Including Exchange and Correlation Effects. *Phys. Rev.* **1965**, *140*, A1133−A1138.
(43) Anisimov, V. I.; Zaanen, J.; Andersen, O. K. Band Theory and Mott Insulators: Hubbard U Instead of Stoner I. *Phys. Rev. B: Condens. Matter Mater. Phys.* **1991**, *44*, 943−954.
(44) Kresse, G.; Furthmüller, J. Efficient Iterative Schemes for Ab Initio Total-Energy Calculations Using a Plane-Wave Basis Set. *Phys. Rev. B: Condens. Matter Mater. Phys.* **1996**, *54*, 11169−11186.
(45) Kresse, G.; Joubert, D. From Ultrasoft Pseudopotentials to the Projector Augmented-Wave Method. *Phys. Rev. B: Condens. Matter Mater. Phys.* **1999**, *59*, 1758−1775.
(46) Blöchl, P. E. Projector Augmented-Wave Method. *Phys. Rev. B: Condens. Matter Mater. Phys.* **1994**, *50*, 17953−17979.
(47) Perdew, J. P.; Burke, K.; Ernzerhof, M. Generalized Gradient Approximation Made Simple. *Phys. Rev. Lett.* **1996**, *77*, 3865−3868.
(48) Wang, L.; Maxisch, T.; Ceder, G. Oxidation Energies of Transition Metal Oxides within the GGA+U Framework. *Phys. Rev. B: Condens. Matter Mater. Phys.* **2006**, *73*, 195107.
(49) Pavone, M.; Ritzmann, A. M.; Carter, E. A. Quantum-Mechanics-Based Design Principles for Solid Oxide Fuel Cell Cathode Materials. *Energy Environ. Sci.* **2011**, *4*, 4933.
(50) Muñoz-García, A. B.; Sannino, F.; Vitiello, G.; Pirozzi, D.; Minieri, L.; Aronne, A.; Pernice, P.; Pavone, M.; D'Errico, G. Origin and Electronic Features of Reactive Oxygen Species at Hybrid Zirconia-Acetylacetonate Interfaces. *ACS Appl. Mater. Interfaces* **2015**, *7*, 21662−21667.
(51) Muñoz-García, A. B.; Pavone, M. Structure and Energy Level Alignment at the Dye−Electrode Interface in p-Type DSSCs: New Hints on the Role of Anchoring Modes from Ab Initio Calculations. *Phys. Chem. Chem. Phys.* **2015**, *17*, 12238−12246.
(52) Muñoz-García, A. B.; Bugaris, D. E.; Pavone, M.; Hodges, J. P.; Huq, A.; Chen, F.; zur Loye, H.-C.; Carter, E. A. Unveiling Structure−Property Relationships in $Sr_2Fe_{1.5}Mo_{0.5}O_{6-\delta}$, an Electrode Material for Symmetric Solid Oxide Fuel Cells. *J. Am. Chem. Soc.* **2012**, *134*, 6826−6833.
(53) Muñoz-García, A. B.; Tuccillo, M.; Pavone, M. Computational Design of Cobalt-Free Mixed Proton-Electron Conductors for Solid Oxide Electrochemical Cells. *J. Mater. Chem. A* **2017**, *5*, 11825−11833.
(54) Muñoz-García, A. B.; Pavone, M. First-Principles Design of New Electrodes for Proton-Conducting Solid-Oxide Electrochemical Cells: A-Site Doped $Sr_2Fe_{1.5}Mo_{0.5}O_{6-\delta}$ Perovskite. *Chem. Mater.* **2016**, *28*, 490−500.
(55) Grimme, S.; Antony, J.; Ehrlich, S.; Krieg, H. A Consistent and Accurate Ab Initio Parametrization of Density Functional Dispersion Correction (DFT-D) for the 94 Elements H-Pu. *J. Chem. Phys.* **2010**, *132*, 154104.
(56) Barone, V.; Casarin, M.; Forrer, D.; Pavone, M.; Sambi, M.; Vittadini, A. Role and Effective Treatment of Dispersive Forces in Materials: Polyethylene and Graphite Crystals as Test Cases. *J. Comput. Chem.* **2009**, *30*, 934−939.
(57) Pecoraro, A.; Schiavo, E.; Maddalena, P.; Muñoz-García, A. B.; Pavone, M. Structural and Electronic Properties of Defective 2D Transition Metal Dichalcogenide Heterostructures. *J. Comput. Chem.* **2020**, *41*, 1946−1955.
(58) Massaro, A.; Pecoraro, A.; Muñoz-García, A.; Pavone, M. First-Principles Study of Na Intercalation and Diffusion Mechanisms at 2D MoS_2/Graphene Interfaces. *J. Phys. Chem. C* **2021**, *125*, 2276−2286.
(59) Zunger, A.; Wei, S. H.; Ferreira, L. G.; Bernard, J. E. Special Quasirandom Structure. *Phys. Rev. Lett.* **1990**, *65*, 353−356.
(60) Mayer, J.; Montroll, E. Molecular Distribution. *J. Chem. Phys.* **1941**, *9*, 2−16.
(61) van de Walle, A.; Asta, M.; Ceder, G. The Alloy Theoretic Automated Toolkit: A User Guide. *Calphad Comput. Coupling Phase Diagrams Thermochem.* **2002**, *26*, 539−553.
(62) Kim, H.; Yoon, S.; Koo, S.; Lee, J.; Kim, J.; Cho, M.; Kim, D. Importance of Chemical Distortion on the Hysteretic Oxygen Capacity in Li-Excess Layered Oxides. *ACS Appl. Mater. Interfaces* **2022**, *14*, 9057−9065.
(63) Raebiger, H.; Lany, S.; Zunger, A. Charge Self-Regulation upon Changing the Oxidation State of Transition Metals in Insulators. *Nature* **2008**, *453*, 763−766.
(64) Sit, H.-L.; Cohen, R.; Selloni, H.; Selloni, A. Simple, Unambiguous Theoretical Approach to Oxidation State Determination via First-Principles Calculations. *Inorg. Chem.* **2011**, *50*, 10259−10267.
(65) Cramer, C. J.; Tolman, W. B.; Theopold, K. H.; Rheingold, A. L. Variable Character of O-O and M-O Bonding in Side-on (H2) 1:1 Metal Complexes of O_2. *Proc. Natl. Acad. Sci.* **2003**, *100*, 3635−3640.
(66) Sutton, L. E.; Bowen, H. J. M. *Tables of Interatomic Distances and Configuration in Molecules and Ions, Special Edition*; The Chemical Society: London, 1958.
(67) Pavone, M.; Muñoz-García, B.; Ritzmann, M.; Carter, A. First-Principles Study of Lanthanum Strontium Manganite: Insights into Electronic Structure and Oxygen Vacancy Formation. *J. Phys. Chem. C* **2014**, *118*, 13346−13356.
(68) Ritzmann, A. M.; Muñoz-García, A. B.; Pavone, M.; Keith, J. A.; Carter, E. A. Ab Initio DFT+U Analysis of Oxygen Vacancy Formation and Migration in $La_{1-x}Sr_xFeO_{3-\delta}$ (x = 0, 0.25, 0.50). *Chem. Mater.* **2013**, *25*, 3011−3019.
(69) Muñoz-García, A. B.; Ritzmann, A. M.; Pavone, M.; Keith, J. A.; Carter, E. A. Oxygen Transport in Perovskite-Type Solid Oxide Fuel Cell Materials: Insights from Quantum Mechanics. *Acc. Chem. Res.* **2014**, *47*, 3340−3348.
(70) Ponti, G.; Palombi, F.; Abate, D.; Ambrosino, F.; Aprea, G.; Bastianelli, T.; Beone, F.; Bertini, R.; Bracco, G.; Caporicci, M.; Calosso, B.; Chinnici, M.; Colavincenzo, A.; Cucurullo, A.; Dangelo, P.; De Rosa, M.; De Michele, P.; Funel, A.; Furini, G.; Giammattei, D.; Giusepponi, S.; Guadagni, R.; Guarnieri, G.; Italiano, A.; Magagnino, S.; Mariano, A.; Mencuccini, G.; Mercuri, C.; Migliori, S.; Ornelli, P.; Pecoraro, S.; Perozziello, A.; Pierattini, S.; Podda, S.; Poggi, F.; Quintiliani, A.; Rocchi, A.; Scio, C.; Simoni, F.; Vita, A. The Role of Medium Size Facilities in the HPC Ecosystem: The Case of the New CRESCO4 Cluster Integrated in the ENEAGRID Infrastructure. *2014 International Conference on High Performance Computing & Simulation (HPCS)*; IEEE, 2014; pp 1030−1033.

https://doi.org/10.1021/acsaem.2c01455
ACS Appl. Energy Mater. 2022, 5, 10721−10730